MINISTRY OF EDUCATION AND TRAINING
HANOI PEDAGOGICAL UNIVERSITY 2
======*****======

DO CHI NGHIA

THEORETICAL MODELS AND SIMULATIONS OF PLASMONIC NANOSTRUCTURES FOR PHOTOTHERMAL AND BIOSENSING APPLICATIONS

Major: Theoretical and Mathematical Physics
Code: 9 44 01 03

SUMMARY OF DOCTORAL THESIS IN PHYSICS

HA NOI - 2020

Introduction

1. Motivation

Plasmonics is a promising field and has attracted much interest of scientists over the world in the revolution of science and nanotechnology. This field explores the interactions between light and matter through surface plasmon resonance (SPR) for a variety of properties and functions. SPR is the collective stimulation of charge carriers (electrons) at the interface between two materials with positive and negative permittivities, typically a metal and a dielectric. Such electron oscillations can propagate along an interface (Surface Plasmon Polariton, SPP) or be confined on subwavelength regions (localized surface plasmon resonance, LSPR). Once excited, all SPR forms can confine the incident electromagnetic field at a deep subwavelength scale, resulting in a significant enhancement of the local field and allowing control of light below the diffraction limit. SPR's appeal makes plasmonic materials highly applicable in a wide variety of fields, including photonics, chemistry, energy, and life sciences. Specifically, there are applications such as biological and optical sensors, drugs and disease treatments, metamaterials, nano-sized electronic chips (Intel chips are now available to 14 nm), and quantum computer. As a result, over the past two decades, scientific interest in plasmonic and SPR materials has intensified. The great advances in nanotechnology in lithographic techniques and classical wet-chemistry methods allow us to synthetically control the sizes, shapes, dimensions, and surface topologies of plasmonic materials, often with nanometer precision. The fabrication and measurement of experimental samples can be very simple in the conditions of countries with advanced science and technology. But for developing countries, especially Vietnam, the experimental steps take a lot of effort and money. In the extremely limited situation in Vietnam, the theoretical models combining with simulations predicting experimental measurements and suggesting new applications for nanostructures are very important and this is the main research purpose of this thesis. The theoretical models in this thesis also create a bridge to connect theory and experiments, which is in shortage in Vietnam.

2. Thesis purpose

The research purpose of the thesis is to develop current Mie theory to study the plasmonic properties of nanostructures investigated in experiments and simulations. Study of temperature variation of these plasmonic nanostructures under laser illumination, to discover new properties and structures to optimize the efficiency, and

to exploit how to use the photothermal effect of the system in various applications.

3. Research methods

The thesis uses semi-empirical modeling method to study the plasmonic properties of the nanostructures. Specifically, the Mie theory and its improvements are used to determine optical spectra of core-shell nanosystems, especially for nanoparticles and graphene-coated nanoparticles. For composite nanostructure composed of a square lattice of graphene nanodisks on a diamond-like carbon thin film grown on a silicon substrate, we apply quasistatic approximation combined with dipole approximation to determine the polarizability of a single graphene resonator from which the absorption and extinction cross sections can be calculated. Along with that, complicated analytical calculations for photothermal effect have been given that continuum mechanics theory and solving heat transfer and diffusion equations, combining numerical methods, simulation methods and data analysis using Fortran and Matlab software. Compare the results obtained with the experimental data and research results of other authors.

4. Scientific significance of the thesis

The thesis proposes a semi-empirical approach to be able to combine with the experimental groups in Vietnam to explain the results and together propose new applications. Not only stopping at the calculation of Mie theory for core-shell systems with perfectly round and smooth surface, our method allows to perform calculations on core-shell nanostructures with rough surface such as nanoflowers and nanostars. From there, a method to study general photothermal effect for different structures is proposed. This method is quite simple, has been published in prestigious scientific journals and can completely help experimental groups verify data and predict the results of systems that have never been studied. The results obtained by the thesis are scientific and practical significances, have contributed to the general understanding of plasmonic properties and photothermal applications of nanostructures.

5. Structure of thesis

Excluding the introduction, the conclusion and the references, this thesis is divided into 4 chapters:

Chapter 1: Overview of basic theories related to research problems

Chapter 2: Mie theory and photothermal model for core-shell nanostructures

Chapter 3: Plasmonic properties of graphene-based nanostructures in terahertz waves

Chapter 4: Plasmonic photothermal heating of graphene-based nanostructures

Chapter 1

Overview of basic theories related to research problems

This chapter presents a system of the basic theories to construct research model for the surface plasmon effect and the photothermal effect of plasmonic nanostructures. All calculations and developments throughout the thesis are based on the foundational knowledge of this chapter. The important physical quantities and parameters that determine the properties and behaviors of surface plasmons will also be discussed.

1.1 Theoretical model for dielectric function

The dielectric function is the basic physical quantity and characterizes the interaction between a material and the electromagnetic field. The general formula of the dielectric function for all materials can be obtained based on the simple model of classical mechanics that is the harmonic oscillator model as follows

$$\varepsilon(\omega) = 1 + \sum_j \frac{\omega_P^2}{\omega_j^2 - \omega^2 - i\gamma_j\omega} \tag{1.1}$$

where ω_P is plasma frequency. This model is also known as the Drude-Lorentz model as a recognition for the contributions of famous scientists Drude and Lorentz to the model of dielectric functions from the early 20th century.

1.2 Mie theory for optical properties of single-material nanoparticles

Physicist Gustav Mie has come up with a analytical solution for the simplest case: a single metallic spheroid. Mie's theory was later developed by Gans to compute non-spherical nanoparticles. These calculations are only accurate provided that the

particle size is very small relative to the range of the incident wavelength. Not only that, today Mie theory is also developed to calculate the optical spectrum for multilayer systems. Recently, the comparison of the optical spectrum calculated by Mie theory with the solar spectrum has been used to optimize the structure and find new materials suitable for solar cell fabrication. In addition, the calculations based on Mie theory allow quantitative prediction of the temperature increase in solutions containing nanoparticles under laser illumination.

1.2.1 Mie theory for single-material spherical nanoparticles

The solution of Maxwells equations for spherical particles is named after the physicist Gustav Mie. The Mie scattering theory allows describing the scattering of a plane monochromatic wave by a homogeneous sphere surround by a homogeneous medium for any particle radius and of any material. It deals with the problem of the continuity of the tangent component of the total electromagnetic fields fulfilling Maxwell's equations outside and inside the sphere. The fields outside the sphere include the incident field of the plane light wave arriving from a distinct source not included in Maxwell equations. However, Mie scattering theory does not deal with the problem of surface electron density oscillations (surface plasmons) coupled to surface localized electromagnetic fields, although usually positions of successive peaks appearing in light scattering spectra of conducting particles obtained with Mie theory, are interpreted as directly related to positions of surface plasmon resonances. Once the Mie coefficients are determined, we can calculate the extinction, absorption and scattering cross sections or the electromagnetic fields inside and outside of the spherical particle. Mie theory codes were used to simulate the optical properties of spheres nanoparticles. When the dimensions of the particles are smaller than the light wavelength it is possible to employ the so-called quasistatic approximation.

The analytical solution of Mie theory for absorption, scattering, and extinction cross sections of the spherical nanoparticle in a continuous dielectric medium are

$$\begin{aligned} Q_{ext} &= \frac{2\pi}{k_m^2}\sum_{n=1}^{\infty}(2n+1)\mathrm{Re}(a_n+b_n), \\ Q_{scat} &= \frac{2\pi}{k_m^2}\sum_{n=1}^{\infty}(2n+1)\left(|a_n|^2+|b_n|^2\right), \\ Q_{abs} &= Q_{ext}-Q_{scat}, \end{aligned} \tag{1.2}$$

where $k_m = 2\pi\sqrt{\varepsilon_m}/\lambda$, ε_m is the dielectric constant of mediun, and λ is the wavelength of incident light, the Mie scattering coefficients

$$\begin{aligned} a_n &= \frac{\psi_n(x)\psi_n^{'}(mx)-m\psi_n(mx)\psi_n^{'}(x)}{\xi_n(x)\psi_n^{'}(mx)-m\psi_n(mx)\xi_n^{'}(x)}, \\ b_n &= \frac{m\psi_n(x)\psi_n^{'}(mx)-\psi_n(mx)\psi_n^{'}(x)}{m\xi_n(x)\psi_n^{'}(mx)-\psi_n(mx)\xi_n^{'}(x)} \end{aligned} \tag{1.3}$$

where $\psi_n(x) = xj_n(x)$ and $\xi_n(x) = xh_n^{(1)}(x)$ are Riccati-Bessel and Riccati-Hankel functions, respectively, $x = k_m R$ with R is the radius of spherical nanoparticle, $m = \sqrt{\varepsilon(\omega)/\varepsilon_m}$ is the ratio of the refractive index of the nanoparticle to the medium at the frequency ω.

1.2.2 Mie theory for single-material aspherical nanoparticles

The optical absorption cross section of a single-material aspherical nanoparticle can be calculated by the extended Mie-Gans theory

$$Q_{abs} = \frac{2\pi\varepsilon_m^{1/2}}{3\lambda}\mathrm{Im}[\alpha_a + \alpha_b + \alpha_c] \tag{1.4}$$

where α_j is the polarizability of the ellipsoid along j direction, where $j = a, b, c$ refers to characteristic lengths of the ellipse, and a and c are the semi-major and semiminor axis, respectively. The calculations have also been widely applied to explain the absorption spectrum of nanorod as the spheroid is prolate. According to the extended Mie theory, α_j is expressed by

$$\alpha_j = \frac{4\pi abc}{3}\frac{\varepsilon(\omega) - \varepsilon_m}{\varepsilon_m + L_j[\varepsilon(\omega) - \varepsilon_m]} \tag{1.5}$$

where L_j is a factor responsible for the ellipsoid shape.

1.3 Basic theory for heating system by plasmon mechanism

1.3.1 Plasmonic heating of single nanoparticle under laser illumination

When metal nanoparticle irradated by laser light, the electrons on surface of nanoparticle are collectively excited and the nanoparticle absorb optical energy and dissipate to the heat. The temperature field in the vicinity of nanoparticle is quasistatic. Therefore, we obtain

$$\kappa\frac{1}{r^2}\frac{\partial}{\partial r}\left(r^2\frac{\partial T}{\partial r}\right) + \frac{3Q_{abs}I_0}{4\pi R^3} = 0 \ \text{ at}\, r < R, \tag{1.6}$$

$$\frac{1}{r^2}\frac{\partial}{\partial r}\left(r^2\frac{\partial T}{\partial r}\right) = 0 \ \text{ at}\, r > R, \tag{1.7}$$

where κ is the thermal conductivity of the medium. The surface temperature increase of nanoparticle ΔT can be easily determined from energy equilibrium conditions, namely, $Q_{abs}I_0 = -4\pi R^2\kappa\partial T/\partial r$ at $r = R$, the results are obtained in the following expression

$$\Delta T = \frac{I_0\, Q_{abs}}{4\pi R\kappa} \tag{1.8}$$

1.3.2 Photothermal heating of solutions due to plasmonic nanoparticles under laser illumination

Laser light with a wavelength in the NIR region can penetrate water and biological tissue to excite the surface localized resonance of metal nanostructures. The nanostructures absorb optical energy and dissipate to the heat. We assume that the efficiency of the light-to-heat conversion is 100% and the particles are randomly distributed in an effective spherical region of radius R. The radius R is estimated by a radius of a sphere with a volume of measured suspensions. The temperature rise in the experimental samples under the laser light illumination is described by two distinct but strongly correlated processes: heat dissipation from particles and the convective heat transfer in medium. The time-dependent temperature increase of experimental samples $\Delta T(r,t)$ induced by the photothermal effect is theoretically described by the Pennes bioheat transfer equation in spherical coordinates

$$\frac{1}{\kappa}\frac{\partial \Delta T}{\partial t} = \frac{1}{r^2}\frac{\partial}{\partial r}\left(r^2\frac{\partial \Delta T}{\partial r}\right) - \frac{\Delta T}{\kappa\tau} + \frac{A}{k}, \tag{1.9}$$

where k and $\kappa = k/(\rho c)$ are the thermal conductivity and thermal diffusivity of the medium, respectively, ρ is the mass density, c is the specific heat, and τ is the perfusion time constant, $A = NQ_{abs}I_0$ is the heat source density due to absorbed energy on metal nanoparticles, N is the number of particles per unit volume in the samples, and I_0 is an irradiation intensity. The temperature variation and its spatial derivatives have to be continuous at $r = R$. The temperature at the center of the localized spherical domain of nanoparticles is assumed to be measured using thermal probes. The temperature at $r = 0$ is

$$\begin{aligned}\Delta T(r=0,t) &= \frac{A}{k}[-\kappa\int_0^t e^{-t'/\tau}\mathrm{erfc}\left(\frac{R}{2\sqrt{\kappa t'}}\right)dt' \\ &- R\int_0^t e^{-t'/\tau}\sqrt{\frac{\kappa}{\pi t'}}\exp\left(\frac{-R^2}{4\kappa t'}\right)dt' \\ &+ \kappa\tau(1-e^{-t/\tau})].\end{aligned} \tag{1.10}$$

1.4 Conclusion

In this chapter, we have presented an overview of the dielectric function theory, the plasmonic properties of materials under electromagnetic field irradiated. Then we presented the general Mie theory to calculate the optical spectra for single-material spherical nanoparticles, for aspherical materials such as nanodisk and nanorod. From here, establish a theoretical calculation method for the temperature increase of the and of the biological solution or tissue containing a set of nanoparticles that are uniformly distributed throughout the system under laser illumination.

Chapter 2

Mie theory and photothermal model for core-shell nanostructures

This chapter presents Mie theory and photothermal model in core-shell nanosystems and its limitations when compared with experiments. In section 2.1, we will present the total Mie theory for core-shell nanosystems with perfectly round and smooth surface and its photothermal effect. The section 2.2 presents optical properties and the thermal-induced stress in the surroundings of heated $Ag@Fe_3O_4$ nanoflowers in different media using the Mie theory and continuum mechanics theory. The content of this section is in the first paper in the thesis-related publications, which was published in *Journal of the Physical Society of Japan*.

2.1 Spherical core-shell nanoparticles

2.1.1 Mie theory for optical spectra

Exact expressions of the Mie scattering theory calculating the extinction, scattering, and absorption cross sections of isotropically coated spherical nanoparticles are given by

$$\begin{aligned} Q_{ext} &= \frac{2\pi}{k_m^2}\sum_{n=1}^{\infty}(2n+1)\mathrm{Re}\left(a_n+b_n\right), \\ Q_{scat} &= \frac{2\pi}{k_m^2}\sum_{n=1}^{\infty}(2n+1)\left(|a_n|^2+|b_n|^2\right), \\ Q_{abs} &= Q_{ext}-Q_{scat}, \end{aligned} \tag{2.1}$$

where

$$a_n = -\frac{U_n^{TM}}{U_n^{TM} + iV_n^{TM}}, \quad b_n = -\frac{U_n^{TE}}{U_n^{TE} + iV_n^{TE}},$$

$$U_n^{TM} = \begin{vmatrix} j_n(k_cR_c) & j_n(k_sR_c) & y_n(k_sR_c) & 0 \\ \frac{\Psi_n^{'}(k_cR_c)}{\varepsilon_c} & \frac{\Psi_n^{'}(k_sR_c)}{\varepsilon_s} & \frac{\Phi_n^{'}(k_sR_c)}{\varepsilon_s} & 0 \\ 0 & j_n(k_sR_s) & y_n(k_sR_s) & j_n(k_mR_s) \\ 0 & \frac{\Psi_n^{'}(k_sR_s)}{\varepsilon_c} & \frac{\Phi_n^{'}(k_sR_s)}{\varepsilon_s} & \frac{\Psi_n^{'}(k_mR_s)}{\varepsilon_m} \end{vmatrix},$$

$$V_n^{TM} = \begin{vmatrix} j_n(k_cR_c) & j_n(k_sR_c) & y_n(k_sR_c) & 0 \\ \frac{\Psi_n^{'}(k_cR_c)}{\varepsilon_c} & \frac{\Psi_n^{'}(k_sR_c)}{\varepsilon_s} & \frac{\Phi_n^{'}(k_sR_c)}{\varepsilon_s} & 0 \\ 0 & j_n(k_sR_s) & y_n(k_sR_s) & y_n(k_mR_s) \\ 0 & \frac{\Psi_n^{'}(k_sR_s)}{\varepsilon_c} & \frac{\Phi_n^{'}(k_sR_s)}{\varepsilon_s} & \frac{\Phi_n^{'}(k_mR_s)}{\varepsilon_m} \end{vmatrix}, \tag{2.2}$$

where R_c and R_s are the inner and outer radius of the core-shell nanostructure, respectively, V_n and U_n are determinants, $j_n(x)$ is the spherical Bessel function of the first kind, $y_n(x)$ is the spherical Neumann function, and $\Psi(x) = xj_n(x)$ and $\xi_n(x) = xy_n(x)$ are the Riccati-Bessel functions. U_n^{TE} and V_n^{TE} are obtained by replacing the dielectric function in Eq.(2.2) with the permeability. The dielectric functions of core, shell, and surrounding medium of the core-shell nanoparticles are ε_c, ε_s and ε_m, respectively.

2.1.2 Photothermal effect in the core-shell nanosystems under near-infrared laser irradiation

Temperature variation of experimental samples $\Delta T(r,t)$ induced by the photothermal effect of gold materials is theoretically described by the Pennes bioheat transfer equation in spherical coordinates Eq.(1.9). The steady-state temperature increase can be estimated using

$$\begin{aligned} \Delta T &= 2\Delta T_{max} R_s N A_{beam} \ln\left[\frac{l_{opt}}{R_{beam}}\right], \\ \Delta T_{max} &= \frac{Q_{abs} I_0}{4\pi k R_s}, \end{aligned} \tag{2.3}$$

where ΔT_{max} is the maximum temperature at the nanoparticle surface, l_{opt}t is the optical path length.

2.2 Plasmonic properties and thermal-induced stress of nanoflowers

In recent years, peculiar properties of composite nanostructures have become of great interest because they have various technological and biomedical applications. The development of nanoscience allows the synthesis of a variety of hybrid systems with desired sizes and structures enabling the designing and creation of multifunctional and complex systems. Magnetite nanoparticles possess novel characteristics such as strong sensitivity to magnetic fields, high biocompatibility and relatively low toxicity in human body, along with capability of removing heavy metal ions. While the localized surface plasmon resonances of silver nanoparticles greatly enhance electric field around the nanostructures and induce other fascinating features in visible range. Silver nanoparticles are also known as effectively antibacterial agents but toxic metal. Local heating of Ag@Fe_3O_4 nanocomposites using both photothermal and magnetic hyperthermia effects have been demonstrated to remarkably increase a rapid temperature rise compared to the single method, and can be used for cancer treatment. Moreover, the localized heat generates spatiotemporally heterogeneous temperature distribution and can improve ultrasonic imaging. Consequently, combining Ag and Fe_3O_4 has considerably enlarged desirable synergistic and complementary effects. In this section, we theoretically investigate optical properties and thermal-induced stress of Ag@Fe_3O_4 core-shell nanoflowers (Fig.2.1), which has been experimentally synthesized in visible range.

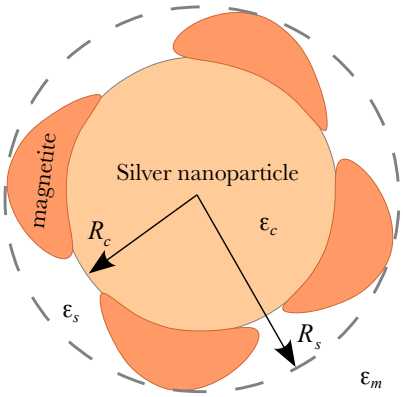

Figure 2.1: Schematic illustration of Ag@Fe_3O_4 nanoflowers.

2.2.1 Mie theory for optical spectra of Ag@Fe_3O_4 nanoflowers

The expressions of the Mie scattering theory calculating the extinction, scattering, and absorption cross section of core-shell nanoflowers are determined by Eqs. (2.1) and (2.2). In the nanoflowers synthesized as shown in Fig.2.1, the iron oxide

petals are grown on silver surface, thus the shell includes Fe_3O_4 and medium. In order to simplify calculations, we use the effective-medium approximation for the shell layer. The effective dielectric function can be modeled by the Lichtenecker model $\varepsilon_s(\omega) = f\varepsilon_{Fe_3O_4} + (1-f)\varepsilon_m$, where f is the fraction of magnetite comprising the shell. While $\varepsilon_c(\omega) = \varepsilon_{Ag}(\omega)$. $R_c = 24$ nm is a radius of the silver core and $R_s = 60$ nm is an outer radius of the nanoflower.

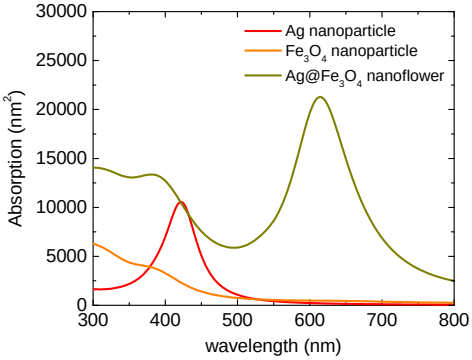

Figure 2.2: Absorption cross sections of Ag, Fe_3O_4, and Ag@Fe_3O_4 nanoparticles in water ($\varepsilon_m = 1.77$) calculated by general Mie theory.

Figure 2.2 shows theoretical calculations using the Mie theory for the absorption spectrum of Ag@Fe_3O_4 nanoflowers, pure spherical Ag and Fe_3O_4 nanoparticles dispersed in water. The resonance peak wavelength of silver nanoparticles with a radius of 24 nm is around 415 nm. The surface plasmon resonance of silver and the electronic transition of magnetite at 400 nm are mainly responsible for the first band of Ag@Fe_3O_4 nanoflowers. While the 2.2 eV (∼565 nm) band gap of magnetite nanostructure significantly reduces the effects of lower energy excitations on the absorption spectrum, it results in an absence of an optical maximum of Fe_3O_4 nanoparticles experimentally observed and theoretically calculated in visible range. When magnetite is coated on the surface of silver nanoparticles, the surface defects can narrow the band gap of magnetite petal and lead to the occurence of the second peak in the absorption spectrum of Ag@Fe_3O_4 nanocomposites. Within the framework of the Mie theory, the dielectric function of Fe_3O_4 is integrated in Q_{abs} via spatial averaging. Consequently, the second band can be interpreted as geometric effects and the interfacial interaction plays minor role in the absorption spectrum. To have the best agreement between our theoretical calculations and previous experiment, an adjustable parameter f is altered to achieve the second peak at 620 nm (close to 615 nm in experiment) and the 620 nm absorbance higher than the 400 nm resonance by a factor of 1.5. Based on these criteria, magnetite is found to cover 40% volume of the shell ($f \approx 0.4$).

Figure 2.3 presents how the absorption spectra of nanoflowers in silica are altered when the magnetite size varies ($R_c = 24$ nm). When replacing water medium with silica, the small dielectric constant difference leads to a red-shift in the second plas-

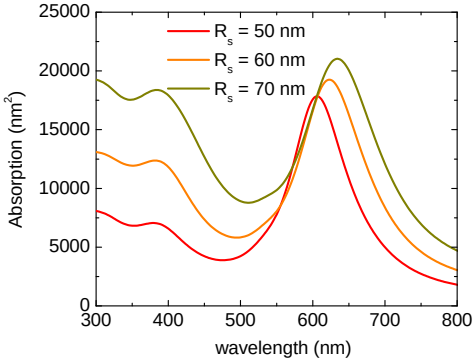

Figure 2.3: Absorption cross sections of $Ag@Fe_3O_4$ nanoflowers calculated by general Mie theory in SiO_2 ($\varepsilon_m = 2.25$) with different shell sizes.

monic resonance toward the near-infrared region and a relatively small blue-shift in the first absorption peak. An increase in the thickness of the Fe_3O_4 layer remarkably increases the absorption intensity near 400 nm wavelength due to coupling between the electronic transitions of magnetite and the plasmon band of silver.

2.2.2 Thermal Strain of $Ag@Fe_3O_4$ nanoflowers

As the $Ag@Fe_3O_4$ suspension is exposed to 400-nm laser light, nanoflowers absorb optical energy at the plasmonic resonant wavelength and effectively generate heat. For the steady state, the distribution of the radially symmetric temperature rise outside a nanoflower ($r \geq R_s$) is given

$$T(r) = \frac{Q_{abs} I_0}{4\pi\kappa_m} \frac{1}{r} = T_s \frac{R_s}{r}, \tag{2.4}$$

where $\kappa_m = 0.6\, W m^{-1} K^{-1}$ is the thermal conductivity of water, T_s is the temperature rise on the surface of the nanoflower, and I_0 is the intensity of the exposing laser light. The temperature profile inside nanoflowers can be obtained using the heat diffusion conditions at interfaces

$$T(r) = \begin{cases} -T_s \left[\dfrac{\kappa_m r^2}{2\kappa_c R_s^2} - \dfrac{2\kappa_s + \kappa_m}{2\kappa_s} + \dfrac{R_c^2 \kappa_m (\kappa_c - \kappa_s)}{2R_s^2 \kappa_s \kappa_c} \right] & \text{in core} \\ T_s \left[-\dfrac{\kappa_m r^2}{2\kappa_s R_s^2} + \dfrac{2\kappa_s + \kappa_m}{2\kappa_s} \right] & \text{in shell} \end{cases} \tag{2.5}$$

Since nanoflowers are modeled to be a roughly spherical shape and are subject to thermal gradients, we assume the deformation induced by thermoelastic effects is spherically symmetric and purely radial. Another assumption is that the coreshell structures can be considered as a homogeneous nanosphere with the radius R_s. The equilibrium equation for isotropic and homogeneous materials in absence of body

forces provides

$$G_j \bigtriangledown^2 \mathbf{u}_j + \left(K_j + \frac{G_j}{3}\right) \bigtriangledown (\bigtriangledown \mathbf{u}_j) - \alpha_j K_j \bigtriangledown T = 0, \tag{2.6}$$

where α is the coefficient of thermal expansion, $\mathbf{u} \equiv \mathbf{u}(r)$ is the strain field, $K_j = E_j/3(1-2\nu_j)$ and $G_j = E_j/2(1+\nu_j)$ are the bulk and shear modulus of medium j $(j = c, s, m)$, respectively, $\nu_j = (3K_j - 2G_j)/2(3K_j + G_j)$ is the Poisson's ratio, and E_j is the Young's modulus. The equilibrium equation associated with $\bigtriangledown \times \mathbf{u}_j = 0$ (no rotation) can reduce to be

$$\bigtriangledown^2 \mathbf{u}_j = \alpha_j \frac{1+\nu_j}{3(1-\nu_j)} \bigtriangledown T(r). \tag{2.7}$$

The deformation field within core $u_c(r)$ and shell $u_s(r)$, and outside $[u_m(r)]$ nanoflowers can be obtained by solving Eq.(2.7), using the finiteness of strain field fields at $r = 0$ and $r = \infty$

$$\begin{aligned} u_c(r) &= A_c r, \\ u_s(r) &= -\alpha_s \frac{1+\nu_s}{3(1-\nu_s)} \frac{\kappa_m T_s}{2\kappa_s R_s^2} \frac{r^3}{5} + A_s r + \frac{B_s}{r^2}, \\ u_m(r) &= \frac{T_s R_s}{2} \frac{\alpha_m (1+\nu_m)}{3(1-\nu_m)} + \frac{B_m}{r^2}, \end{aligned} \tag{2.8}$$

where coefficients A_c, A_s, B_s and B_m can found by applying continuity of traction and fields across interfaces.

Substituting the strain displacements into the stressstrain relations gives the radial stresses in regions

$$\begin{aligned} \sigma_{c,rr}(r) &= 3K_c A_c, \\ \sigma_{s,rr}(r) &= -K_s \alpha_s \frac{3-\nu_s}{1-\nu_s} \frac{\kappa_m T_s}{2\kappa_s R_s^2} \frac{r^2}{5} + 3K_s A_s - \frac{4G_s B_s}{r^3}, \\ \sigma_{m,rr}(r) &= \alpha_m \frac{\nu_m K_m}{1-\nu_m} \frac{T_s R_s}{r} - \frac{4G_m B_m}{r^3}. \end{aligned} \tag{2.9}$$

Equation (2.9) presents the spatial distribution and strong size dependence of the stress strains. While the radial pressure inside the core remain unchanged, the stresses within the nanoflower shell and in medium are strongly dependent on r.

For water medium, Young's modulus E_m is supposed to be zero, we enable to measure the spatial displacement both stress strains outside nanoflowers. Because $G_m = 0$, $\nu_m = 1/2$, and T_s varies less than 100 ^{o}C, $\sigma_{m,rr}(r) = \alpha_m K_m T_s R_s / r$ is relatively small in comparison with K_m. The radial stress is long-ranged and simply inversely proportional to the distance r.

When the surrounding medium is silica glass, we can determine the stress in silica using 400 nm laser irradiation at a power density of 10^4 W/cm^2 for different sizes

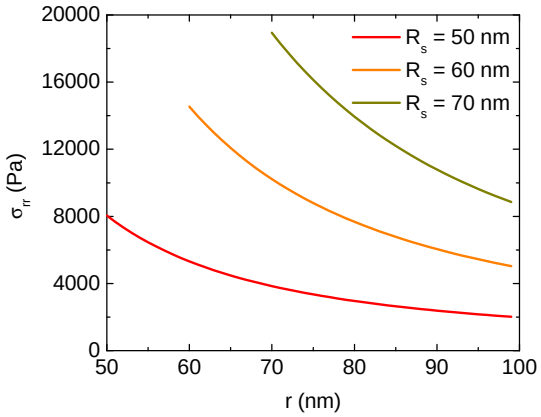

Figure 2.4: The radial stress outside versus distance from center of $Ag@Fe_3O_4$ nanoflowers with various diameters.

of the nanocomposites in Fig.2.4. The stress components in silica decay almost as the inverse cube of the distance near the outer surface but it is proportional to $1/r$ in long-range distances. The variation is identical to the previous finding. If the stress does not obey an inverse cube law, the system may have impurity, obstacles or asymmetrical interrupting factors. As a result, laser-induced thermoelastic effects can be exploited to detect defects in substances and devices.

2.3 Conclusion

We have explored optical properties and the thermal-induced stress in the surroundings of heated $Ag@Fe_3O_4$ nanoflowers in different media using the Mie theory and continuum mechanics theory. Our calculations show that the resonance wavelength of around 400 nm in the absorption is attributed to the surface plasmon resonance of silver and the electronic transition of iron oxide. The second optical band at 620 nm is due to geometrical effects. A subtle interplay between core and shell is supposed to have an inconsiderable effect on the absorption spectrum. The optical peak shift is strongly dependent on the finite size of the nanocomposite and how magnetite is grown on the silver surface. Using laser irradiation or AC magnetic fields leads to temperature rise that generates the strain field inside nanoflowers and their ambient surrounding environment. The thermal stress variation has been analytically found. The long-range stress decays as the inverse of the distance and this finding is in a good agreement with previous study.

Chapter 3

Plasmonic properties of graphene-based nanostructures in terahertz waves

In this chapter, we present the theoretical studies on the plasmonic properties of graphene on bulk substrates and graphene-coated nanoparticles. The surface plasmons of such systems are strongly dependent on bandgap and Fermi level of graphene that can be tunable by applying external fields or doping. An increase of bandgap prohibits the surface plasmon resonance for GHz and THz frequency regime. While increasing the Fermi level enhances the absorption of the graphene-based nanostructures in these regions of wifi-waves. Some mechanisms for electric-wifi-signal energy conversion devices are proposed. The contents of this chapter are in the second paper in the thesis-related publications.

3.1 Theoretical background

3.1.1 Tight binding approach for graphene

Graphene is a two-dimensional material that has carbon atoms arranged in a honeycomb lattice. Let $a = 0.142$ nm be the length of the nearest-neighbor bonds. The two lattice vectors can be expressed by $\mathbf{a}_1 = a(3/2, \sqrt{3}/2)$ and $\mathbf{a}_2 = a(3/2, -\sqrt{3}/2)$.

The Hamiltonian gives the graphene energy band

$$E_{\pm}(\mathbf{k}) = \pm t\sqrt{3 + f(\mathbf{k})}, \tag{3.1}$$

where,

$$f(\mathbf{k}) = 2\cos\sqrt{3}k_y a + 4\cos\left(\frac{\sqrt{3}}{2}k_y a\right)\cos\left(\frac{3k_x a}{2}\right). \tag{3.2}$$

At $\mathbf{K} = (2\pi\sqrt{3}, 2\pi)/3\sqrt{3}a$ and $\mathbf{K'} = (2\pi\sqrt{3}, -2\pi)/3\sqrt{3}a$, $E_\pm = 0$. Near K point, $\mathbf{k} = \mathbf{K} + \mathbf{q}$ with $\mathbf{q}$ relatively small, the electron energy can be calculated by

$$E_\pm = \pm\frac{3t}{2}qa. \tag{3.3}$$

3.1.2 Optical graphene conductivity

The inter- and intra-band conductivity of gapped graphene can be determined by

$$\begin{aligned}
\sigma_{intra} &= \frac{ie^2/\pi\hbar^2}{\omega + i\tau^{-1}} \int_\Delta^\infty dE \left(1 + \frac{\Delta^2}{E^2}\right) [f(E) + 1 - f(-E)] \\
\sigma_{inter} &= \frac{ie^2\omega}{\pi} \int_\Delta^\infty dE \left(1 + \frac{\Delta^2}{E^2}\right) \frac{f(E) - f(-E)}{4E^2 - \hbar^2(\omega + i\Gamma)^2}.
\end{aligned} \tag{3.4}$$

The graphene chemical potential can be controlled by an applied electric field E_d

$$\frac{\pi\varepsilon_0\hbar^2 v_F^2}{e} E_d = \int_0^\infty E[f(E) - f(E + 2E_c)]dE, \tag{3.5}$$

where ε_0 is the vacuum permittivity.

3.2 Absorption of graphene

In order to estimate the absorption of graphene, the reflection and transmission coefficient of graphene on top of semi-infinite substrate must be known. These are

$$\begin{aligned}
r_{TE} &= \frac{k_1 - k_2 - \mu_0\sigma(\omega)\omega}{k_1 + k_2 + \mu_0\sigma(\omega)\omega}, \\
t_{TE} &= \frac{2k_1}{k_1 + k_2 + \mu_0\sigma(\omega)\omega}, \\
r_{TM} &= \frac{\varepsilon_2 k_1 - \varepsilon_1 k_2 + \sigma(\omega)k_1 k_2/\varepsilon_0\omega}{\varepsilon_2 k_1 + \varepsilon_1 k_2 + \sigma(\omega)k_1 k_2/\varepsilon_0\omega}, \\
t_{TM} &= \frac{2\varepsilon_1 k_2}{\varepsilon_2 k_1 + \varepsilon_1 k_2 + \sigma(\omega)k_1 k_2/\varepsilon_0\omega},
\end{aligned} \tag{3.6}$$

where TM and TE denote for the transverse magnetic and electric mode, respectively, μ_0 is the vacuum permeability. $k_m = \sqrt{\varepsilon_m\omega^2/c^2 - k_\parallel^2}$, $k_\parallel$ is the component of wavevector parallel to the surface, ε_m is the dielectric function of medium m. The light comes from medium 1, partly transmits to medium 2 and reflects back into medium 1.

The incident and transmitted light have the intensity $I_0 = \frac{1}{2}\sqrt{\frac{\varepsilon_0}{\mu_0}}|E_0|^2\mathrm{Re}(\varepsilon_1)$ and $I_t = \frac{1}{2}\sqrt{\frac{\varepsilon_0}{\mu_0}}|E_t|^2\mathrm{Re}(\varepsilon_2)$. E_0 and E_t are the amplitude of incident and transmitted

electric fields. Thus, the absorbance of graphene can be calculated by

$$A = 1 - |r|^2 - \mathrm{Re}\left(\frac{\sqrt{\varepsilon_2}}{\sqrt{\varepsilon_1}}\right)|t|^2. \tag{3.7}$$

3.3 Numerical results and discussions

3.3.1 Absorption spectra of freely-suspended graphene

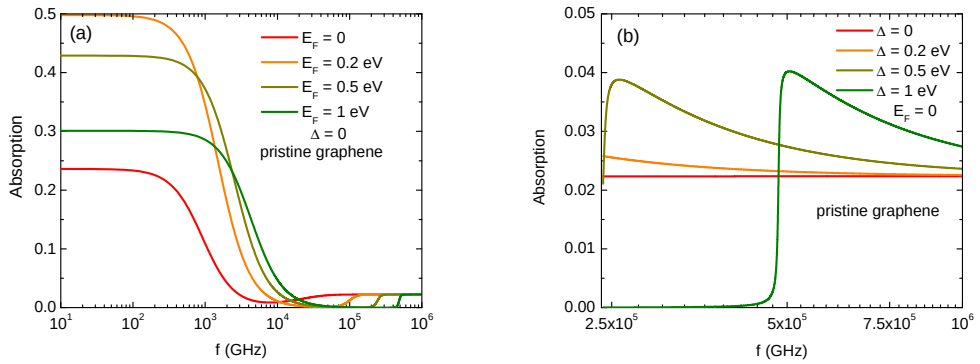

Figure 3.1: Normal-incidence absorption spectra of free-standing graphene with (a) different Fermi energies when $\Delta = 0$, and (b) different values of band gap at $E_F = 0$.

Figure 3.1 presents the absorption spectra of freely-suspended graphene with a variety of chemical potentials and band gaps. In visible light regions, our results are in good agreement with previous results with $\sigma(\omega) = \sigma_0$, $A \approx \pi\alpha \approx 2.3$ % and $T \approx 97.7\%$. Graphene is extremely transparent in air. This finding suggests that $\sigma(\omega)$ and the absorption remain constant and can be significantly enhanced by increasing E_F. Interestingly, approximately 50% of the optical energy of the incidence light can be absorbed by graphene when $E_F = 1$ eV.

3.3.2 Absorption spectra of a monolayered graphene on bulk substrates

As can be seen in 3.2, the absorption of graphene on gold semi-infinite substrate in air, free electrons on the gold surface absorb and re-emit the most incident photons. This result suggests that pure graphene has a higher absorption than graphene on gold substrates. $|r| \approx 1$ at low frequencies since $\varepsilon_2(\omega) \to \infty$, while $\varepsilon_1(\omega) = 1$ and $g(\omega)$ are finite values.

Figure 3.3 presents the absorption cross section of a graphene sheet on silica substrate. Silica substrates have been broadly used to support graphene sheets in many experiments and devices. Graphene on SiO_2 also absorbs less electromagnetic energy but the absorbance ranges from 15% to 37% as E_F and Δ approach 0. Note

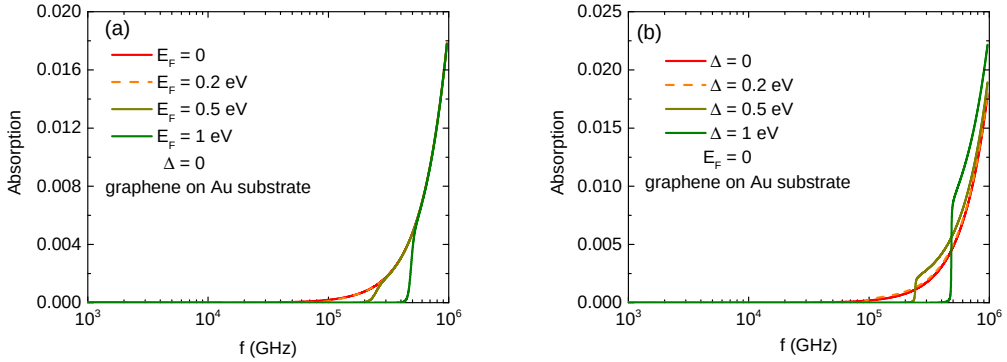

Figure 3.2: Normal-incidence absorption spectra of a monolayer graphene on gold substrate with (a) different Fermi energies when $\Delta = 0$, and (b) different values of band gap at $E_F = 0$.

that the nonzero bandgap induces a significant reduction of absorption at low energy. Reducing Δ as much as possible maximizes the performance of the plasmon in graphene.

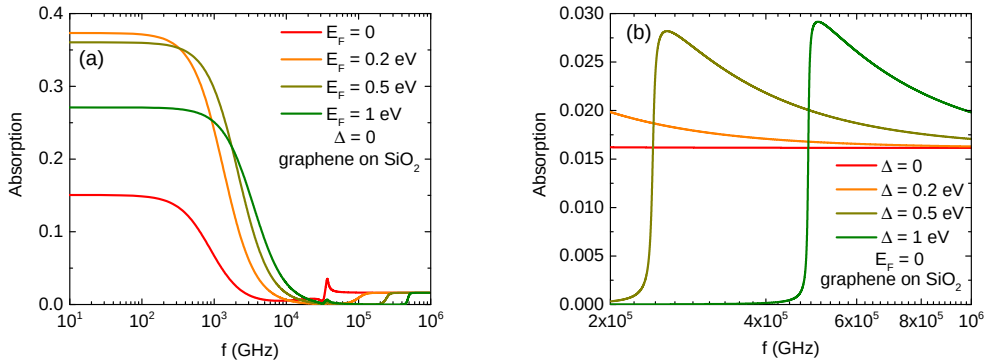

Figure 3.3: Normal-incidence absorption spectra of a monolayered graphene on silica substrate with (a) different Fermi energies when $\Delta = 0$, and (b) different values of band gap at $E_F = 0$.

3.3.3 Absorption spectrum of graphene-coated SiO_2 nanoparticles

The absorption cross section A_{abs} of graphene-conjugated silica nanoparticle with a radius R is given using the Mie theory

$$
\begin{aligned}
a_l &= \frac{\Psi_l(\frac{2\pi n_m R}{\lambda})\Psi_l'(\frac{2\pi n_p R}{\lambda}) - \frac{n_p}{n_m}\Psi_l'(\frac{2\pi n_m R}{\lambda})\Psi_l(\frac{2\pi n_p R}{\lambda}) - i\sigma\sqrt{\frac{\mu_0}{\varepsilon_0\varepsilon_m}}\Psi_l'(\frac{2\pi n_m R}{\lambda})\Psi_l'(\frac{2\pi n_p R}{\lambda})}{\xi_l(\frac{2\pi n_m R}{\lambda})\Psi_l'(\frac{2\pi n_p R}{\lambda}) - \frac{n_p}{n_m}\xi_l'(\frac{2\pi n_m R}{\lambda})\Psi_l(\frac{2\pi n_p R}{\lambda}) - i\sigma\sqrt{\frac{\mu_0}{\varepsilon_0\varepsilon_m}}\xi_l(\frac{2\pi n_m R}{\lambda})\Psi_l(\frac{2\pi n_p R}{\lambda})}, \\
b_l &= \frac{n_p}{n_m}\frac{\Psi_l(\frac{2\pi n_m R}{\lambda})\Psi_l'(\frac{2\pi n_p R}{\lambda}) - \Psi_l'(\frac{2\pi n_m R}{\lambda})\Psi_l(\frac{2\pi n_p R}{\lambda}) - i\sigma\sqrt{\frac{\mu_0}{\varepsilon_0\varepsilon_m}}\Psi_l'(\frac{2\pi n_m R}{\lambda})\Psi_l'(\frac{2\pi n_p R}{\lambda})}{\frac{n_p}{n_m}\xi_l(\frac{2\pi n_m R}{\lambda})\Psi_l'(\frac{2\pi n_p R}{\lambda}) - \xi_l'(\frac{2\pi n_m R}{\lambda})\Psi_l(\frac{2\pi n_p R}{\lambda}) - i\sigma\sqrt{\frac{\mu_0}{\varepsilon_0\varepsilon_m}}\xi_l(\frac{2\pi n_m R}{\lambda})\Psi_l(\frac{2\pi n_p R}{\lambda})}, \\
A_{abs} &= \frac{\lambda^2}{2\pi\varepsilon_m}\sum_{l=1}^{\infty}(2l+1)\left(Re(a_l+b_l) - |a_l|^2 - |b_l|^2\right), \qquad (3.8)
\end{aligned}
$$

where $n_p = \sqrt{\varepsilon_{SiO_2}}$ is the complex refractive index of the nanoparticle, $n_m = \sqrt{\varepsilon_m} = 1$ is the refractive index of vacuum, $\Psi_l(x) = xj_l(x)$ and $\xi_l(x) = xh_l^{(1)}(x)$ are Riccatie-Bessel and Riccatie-Hankel functions, respectively, $j_l(x)$ is the spherical Bessel function of the first kind, and $h_l^{(1)}(x)$ is the spherical Hankel function of the first kind.

Figure 3.4 shows the absorption cross section of a graphene-coated 50-nm-radius SiO_2 nanoparticle. It is easy to see that two plasmonic resonances of graphene/SiO_2 nanoparticle are in the reliable range of the quasi-static approximation but non-zero optical conductivity of graphene layer on nanoparticle's surface leads to the failure of the approximation. Two peaks in the spectrum are attributed to the transitions of the electrons in graphene and frequencies of longitudinal and transverse optical phonons of SiO_2. The position of the first resonance is strongly sensitive to E_F and the size of nanoparticle. The chemical potential enhancement weakens the contribution of graphene on the absorption spectrum. Technological advances have allowed the precise measuring of the particle's size. Interestingly, the absorption difference between the two optical peaks is about 1-2 orders of magnitude. This phenomenon is reversed in the bulk system.

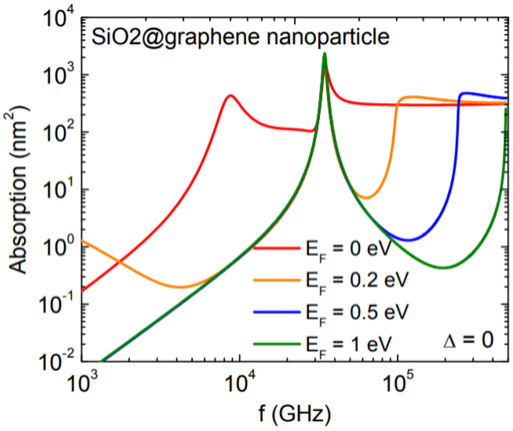

Figure 3.4: Absorption spectrum of graphene-coated SiO_2 nanoparticle with $R = 50$ nm and various Fermi levels.

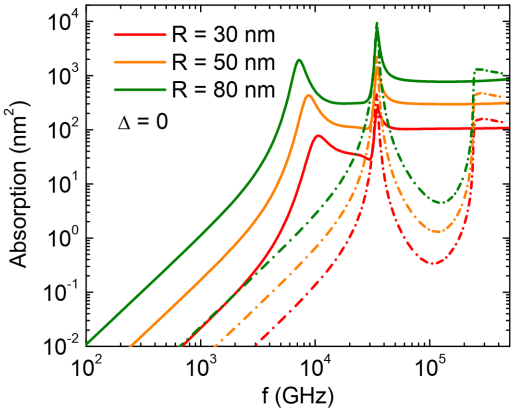

Figure 3.5: Absorption spectrum of graphene-coated SiO_2 nanoparticle with $R = 30$ (red), 50 (orange) and 80 nm (green) at different chemical potentials. The solid and dashed-dotted lines correspond to $E_F = 0$ and 0.5 eV, respectively.

The strong dependence of the particle size on the optical spectrum is shown in Fig. 3.5. The first peak resonant position is blueshifted with increasing particle size. The magnitude of the plasmonic resonant peaks decays remarkably when the radius is reduced. The second band's position remains unchanged as varying sizes and E_F of graphene since it is just dependent on phonon properties of silica.

3.4 Conclusion

In this chapter, we have studied the absorption spectrum of graphene-based systems. Graphene is quite transparent when it is put on gold substrates because the metallic substrate reflects most of the electromagnetic wave energy. The silica substrate allows approximately 15-37% incident wave energy to be absorbed on graphene. A variation of the absorbed energy depends on the Fermi energy and

bandgap of graphene. The strong absorbance of graphene in the GHz-THz regime can be exterminated by increasing the bandgap. The plasmonic properties of the nanostructures are demonstrated to be much larger than that in their bulk counterparts. Two peaks in the absorption spectrum of graphene-coated silica nanoparticle can be used to produce energy converters using the plasmo-electric effect.

Chapter 4

Plasmonic photothermal heating of graphene-based nanostructures

In this chapter, we present a theoretical model to calculate plasmonic properties of graphene-based nanostructures and temperature distribution in the systems when irradiated by a mid-infrared laser light. Our graphene-based systems are composed of a square lattice of graphene nanodisks on a diamond-like carbon thin film grown on a silicon substrate. Optical resonances are sensitive to structural parameters and the number of graphene layers. Under mid-infrared laser irradiation, the steady-state temperature gradients are calculated. Furthermore, the analytical formulas that we give show a close correlations between temperature change and the optical power, laser spot, and thermal conductivity of dielectric layer. The content of this chapter is in the third paper in the thesis-related publications, which was published in *Physica Status Solidi-Rapid Research Letters*.

4.1 Motivation

Graphene has been recently considered as a novel plasmonic material, which strongly confines electromagnetic fields but provides relatively low loss. Consequently, graphene-based metamaterials are of interest and potentially display various intriguing behaviors.

4.2 Plasmonic properties and temperature distribution of graphene-based nanostructures

Our graphene-based systems are investigated as shown in figure 4.1.

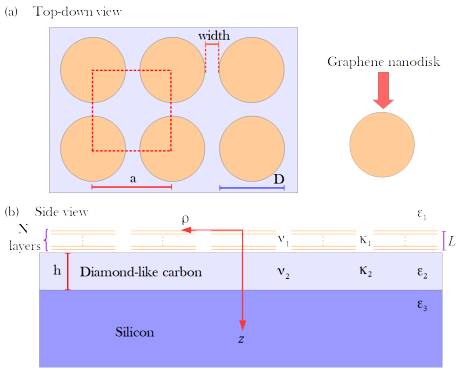

Figure 4.1: (a) The top-down view and b) the side view of graphene-based system including structural parameters.

The reflection and transmission coefficient of the graphene-based nanostructure are

$$\begin{aligned} t_{13} &= \frac{t_{12}t_{23}e^{i\left(\frac{\omega}{c}\sqrt{\varepsilon_2}h\right)}}{1+r_{12}r_{23}e^{2i\left(\frac{\omega}{c}\sqrt{\varepsilon_2}h\right)}}, \\ r_{13} &= \frac{r_{12}+r_{23}e^{2i\left(\frac{\omega}{c}\sqrt{\varepsilon_2}h\right)}}{1+r_{12}r_{23}e^{2i\left(\frac{\omega}{c}\sqrt{\varepsilon_2}h\right)}} \end{aligned} \tag{4.1}$$

where c is the speed of light, $g \approx 4.52$ is the net dipolar interaction over the whole square lattice, r_{pq} and t_{pq} are the bulk reflection and transmission coefficients, respectively, when electromagnetic fields strike from medium p to q. From these, we compute the transmission $|t_{13}|^2 \equiv |t_{13}(N)|^2$ for $N > 0$ and $N = 0$ corresponding to systems with and without graphene plasmonic resonators. The extinction spectra measured in the experiments is the relative difference in these transmissions $1\text{-}|t_{13}(N)|^2/t_{13}(N=0)|^2$. The calculations clearly determine confinement effects of electromagnetic fields due to graphene plasmons. Figure 4.2 shows theoretical in-

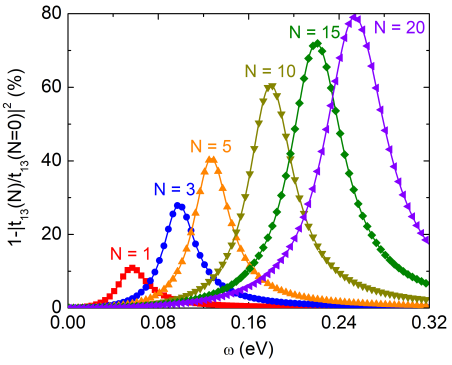

Figure 4.2: Theoretical extinction spectra for systems having a graphenedisk array with $E_F = 0.45$ eV and $\hbar\tau^{-1} = 0.03$ eV at several numbers of graphene layers.

frared extinction spectra of graphene-based systems with several values of graphene

plasmon layers. The numerical results indicate the plasmonic peak for a square lattice of three-layer-graphene disks is roughly located at 0.1 eV, which quantitatively agrees with experiment. The presence of graphene plasmons reduces the transmission of electromagnetic fields through these systems. An inrease in N blue-shifts the plasmonic resonance and enhances the amplitude signal in the optical spectra. More mid-infrared optical energy is confined in the system as increasing the layer number of graphene plasmons. The amount of the trapped energy can be indirectly measured via temperature caused by the light-to-heat conversion process.

Under infrared laser irradiation, the diamon-like carbon layers and graphene-disk resonators absorb electromagnetic energy and are heated up. The temperature increase in cylinderical coordinate, $\Delta T \equiv \Delta T(\rho, z)$, obeys the heat diffusion equation. Because the graphene resonator is a 2D material, the thermal conductivity is anisotropic. This diffusion equation in the layer including all stacked plasmonic disks is

$$\kappa_{1\parallel}\frac{1}{\rho}\frac{d}{d\rho}\left(\rho\frac{d\Delta T}{d\rho}\right)+\kappa_{1\perp}\frac{d^2\Delta T}{dz^2}=p_0 e^{-\frac{2\rho^2}{w^2}}e^{-\nu_1 z}, \tag{4.2}$$

where p_0 is the laser power per unit volume, w is the laser spot, ν_1 is the absorption coefficient, $\kappa_{1\parallel}$ and $\kappa_{1\perp}$ are the effective in-plane and out-of-plane thermal conductivity, respectively. In the diamond-like layer, the diffusion equation is

$$\kappa_2\left[\frac{1}{\rho}\frac{d}{d\rho}\left(\rho\frac{d\Delta T}{d\rho}\right)+\frac{d^2\Delta T}{dz^2}\right]=p_0 e^{-\frac{2\rho^2}{w^2}}e^{-\nu_1 L-\nu_2(z-L)}, \tag{4.3}$$

where $\kappa_2 \approx 0.6\, W/K/m$ is the thermal conductivity of the diamond-like layer and $\nu_2 \approx 1.5\ \mu m^{-1}$ is the absorption coefficient. For simplification purpose, we assume that the silicon substrate is kept at ambient temperature by contacting with a thermostat. This boundary condition was used to successfully analyze experiments.

To solve these differential equations, we take the Hankel transform of the aforementioned equations in ρ and it gives

$$\begin{aligned}\Theta(u,z) &= A_1(u)e^{-\sqrt{\frac{\kappa_{1\parallel}}{\kappa_{1\perp}}}uz}+B_1(u)e^{\sqrt{\frac{\kappa_{1\parallel}}{\kappa_{1\perp}}}uz}\\ &\quad+\frac{\nu_1 P_0(1-R)}{2\pi(k_{1\parallel}u^2-\kappa_{1\perp}\nu_1^2)}e^{-\frac{u^2w^2}{8}}e^{-\nu_1 z},\ 0\le z\le L \qquad (4.4)\\ \Theta(u,z) &= A_2(u)e^{-uz}+B_2(u)e^{uz}\\ &\quad+\frac{\nu_2 P_0(1-R)}{2\pi\kappa_2(u^2-\nu_2^2)}e^{-\frac{u^2w^2}{8}}e^{-\nu_1 L}e^{-\nu_2(z-L)},\ L\le z\le L+h \qquad (4.5)\end{aligned}$$

where $\Delta T(\rho,z)=\int_0^\infty \Theta(u,z)J_0(\rho u)udu$ with J_0 being the Bessel function of the first kind. P_0 is the power of the incident flux. A correction factor $(1-R)$ implies that only the absorption and transmission component of light play a role in the heating process. The reflection is calculated by $R=|r_{13}|^2$. $A_1(u)$, $B_1(u)$, $A_2(u)$, and $B_2(u)$ are parameters determined by boundary condition.

4.3 Numerical results for the spatial distributions of steady-state temperature increase in graphene-based systems

Numerical results are shown in Figure 4.3 for different N. The incident photons are highly localized at the surface and spatially decay toward the bottom of the diamond-like carbon layer. The temperature increase at the hottest spot area ($z = 0$ and $\rho = 0$) in the case of $N = 10$ is 45 K, whereas that of systems having $N = 3$ and $N = 1$ are approximately 33 K and 34.5 K, respectively. These temperature increases are much higher than $\Delta T(\rho = 0, z = 0) \approx 1.67$ K for the system without graphene plasmons. This result clearly indicates that the dielectric loss is dominated by the ohmic loss (Joule heating) on graphene resonators under the mid-infrared irradiation.

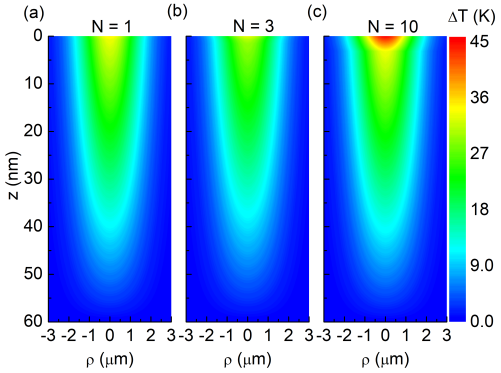

Figure 4.3: Spatial contour plots of the steady-state temperature increase in Kelvin units in graphene-based systems having (a) $N = 1$, (b) $N = 3$, and (c) $N = 10$ under illumination of a quantum cascade laser light.

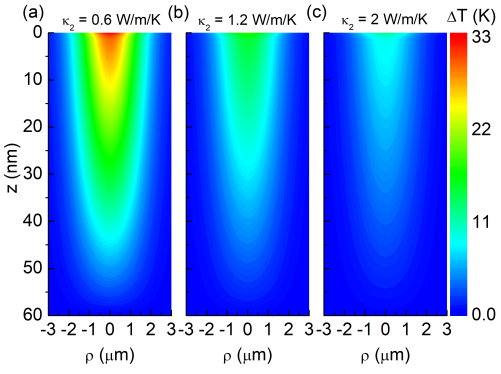

Figure 4.4: Spatial contour plots of the steady-state temperature increase in Kelvin units in graphene-based systems having $N = 3$ and (a) $\kappa_2 = 0.6$ $W/m/K$, (b) $\kappa_2 = 1.2$ $W/m/K$, and (c) $\kappa_2 = 2.0$ $W/m/K$ under illumination of a quantum cascade laser light.

The thermal conductivity of the thin film (κ_2) below graphene plasmons has a significant influence on the temperature increase in graphene-based systems. Figure 4.4 shows that the steady temperature profile of the system for different values of κ_2 illuminated by the mid-infrared laser light. We use the same laser as the calculations in Figure 4.3. The object having a larger κ_2 requires more thermal energy to be heated. Thus, the temperature increase is depressed.

4.4 Conclusion

While illuminating the systems by the mid-infrared laser light, plasmonic nanodisks absorb more optical energy than the counterparts without graphene and convert to thermal dissipation. This finding indicates that the ohmic loss is much larger than the dielectric loss in the mid-infrared regime. An increase in graphene plasmonic layers enhances the thermal gradients. At fixed number of graphene layers, the temperature increase is linearly proportional to the optical power and decays as the inverse square of the laser spot. Furthermore, a decrease in the heated temperature, as increasing the thermal conductivity of the thin film layer, is also calcualted and discussed.

Conclusion

The thesis studies plasmonic properties and photothermal effects of core-shell nanostructures of different shapes and composite nanostructures based on graphene. From the absorption spectra obtained by the Mie theory, we have developed methods for calculating the temperature rise of nanostructures under laser illumination. New academical contributions of the thesis can be summarized as follows:

- Developing the Mie theory studying plasmonic properties (absorption, scattering and extinction spectra) for core-shell nanoparticles. This complete Mie theory can be accurately calculated to a system of 160 nm when it is compared to experimental data.

- Exploring the optical properties and the thermal-induced stress in the surroundings of heated $Ag@Fe_3O_4$ nanoflowers in different media using the Mie theory and continuum mechanics theory. Using laser irradiation leads to temperature rise that generates the strain field inside nanoflowers and their ambient surrounding environment. The thermal stress variation has been analytically found. The long-range stress decays as the inverse of the distance and this finding is in a good agreement with previous study. The stress components in silica decay almost as the inverse cube of the distance near the outer surface. As a result, laser-induced thermoelastic effects can be exploited to detect defects in substances and devices.

- Theoretically study the plasmonic properties of graphene on bulk substrates and graphene-coated nanoparticles. The surface plasmons of such systems are strongly dependent on bandgap and Fermi level of graphene that can be tunable by applying external fields or doping. An increase of bandgap prohibits the surface plasmon resonance for GHz and THz frequency regime. While increasing the Fermi level enhances the absorption of the graphene-based nanostructures in these regions of wifi-waves. Some mechanisms for electric-wifi-signal energy conversion devices are proposed. Our results have a good agreement with experimental studies and can pave the way for designing state-of-the-art electric graphene-integrated nanodevices that operate in GHz-THz radiation.

- Investigating the plasmonic heating of graphene-based systems under irradiation of a mid-infrared laser. The nanostructures comprise a square array of multilayer graphene nanodisks deposited on the diamond-like carbon thin film,

which is supported by a silicon substrate. Our numerical results are in accordance with experiments. While illuminating the systems by the laser light, plasmonic nanodisks absorb more optical energy than the counterparts without graphene and convert to thermal dissipation. This finding indicates that the ohmic loss is much larger than the dielectric loss in the mid-infrared regime. An increase in graphene plasmonic layers enhances the thermal gradients. At fixed number of graphene layers, the temperature increase is linearly proportional to the optical power and decays as the inverse square of the laser spot. Furthermore, a decrease in the heated temperature, as increasing the thermal conductivity of the thin film layer, is also calculated and discussed.

Thesis-related publications

1. Anh D. Phan, Nghia C. Do, and Do T. Nga, "Thermal-induced stress of plasmonic magnetic nanocomposites", *Journal of the Physical Society of Japan* **86**, 084401 (2017).

2. Do T. Nga, Do C. Nghia, Chu V. Ha, "Plasmonic properties of graphene-based nanostructures in terahertz waves", *Journal of Science: Advanced Materials and Devices* **2**, 371-377 (2017).

3. Anh D. Phan, Do T. Nga, Do C. Nghia, Vu D. Lam, and Katsunori Wakabayashi, "Effects of Mid-infrared Graphene Plasmons on Photothermal Heating", *Physica Status Solidi - Rapid Research Letters* **14**, 1900656 (2020).